

Chapter 2

Chemical Vapor Synthesis of Nanocrystalline Oxides

Ruzica Djenadic and Markus Winterer

Abstract The generation of nanoparticles in the gas phase by Chemical Vapor Synthesis (CVS) may be described from the point of view of chemical engineering as a sequence of unit operations among which reactant delivery, reaction energy input, and product separation are key processes which determine the product characteristics and quality required by applications of nanoparticles and powders. In case of CVS, the volatility of the reactants (precursors) may severely limit the possible type of products as well as the production rate. It is shown that these limits can be lifted by use of a laser flash evaporator which also enables the use of precursor mixtures for the production of complex oxides as shown for Co-doped ZnO and the pulsed operation to influence powder characteristics. The mode in which energy is supplied to the particle synthesis reactor has also substantial influence on particle and powder characteristics as is shown for TiO₂ using different time-temperature profiles.

2.1 Introduction

Nanocrystalline oxides are used in ceramics, catalysts, fuel cells, photovoltaic devices, or gas sensors, etc. and can be prepared by a large number of methods each with different advantages and disadvantages [1]. Fumed silica (SiO₂) is the first industrially produced nanostructured material [2] using a gas phase process that has been transferred to other oxides, such as titania (TiO₂), alumina (Al₂O₃), or zirconia (ZrO₂) which allows the tailoring of their properties based on process simulations [3].

In this chapter, we report on new developments of Chemical Vapor Synthesis (CVS), a modified Chemical Vapor Deposition (CVD) method in which the process

R. Djenadic · M. Winterer (✉)

Nanoparticle Process Technology, Faculty of Engineering and CENIDE
(Center for Nanointegration Duisburg-Essen), University of Duisburg-Essen,
Lotharstraße 1, 47057 Duisburg, Germany
e-mail: markus.winterer@uni-due.de

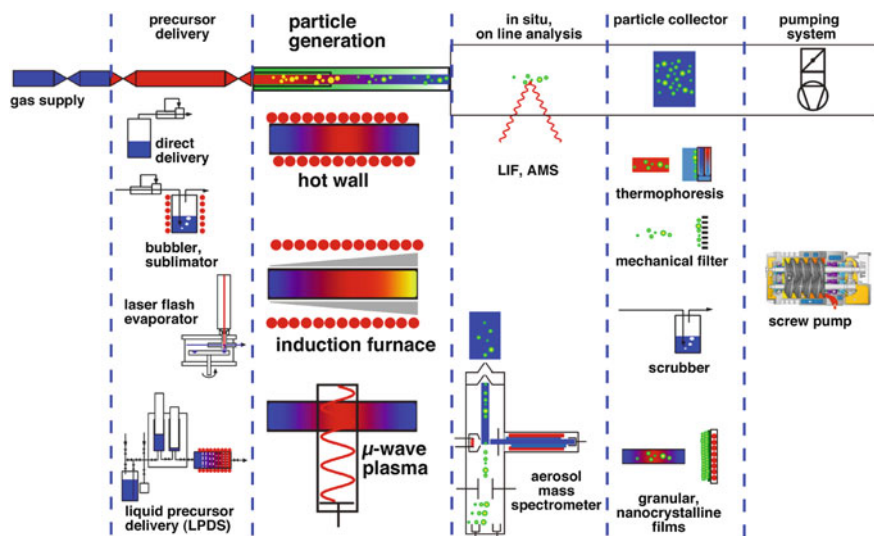


Fig. 2.1 Overview of the modular CVS reactor at the University Duisburg-Essen with different options for the unit operations: precursor delivery, particle generation, process analysis, and particle collection (drawing of screw pump courtesy of Dr.-Ing. K. Busch GmbH)

parameters are adjusted such that (nano-) particles are formed instead of films [4]. In this contribution novel modules for unit operations, relevant for the CVS process such as precursor delivery and energy input are described (Fig. 2.1), as well as their influence on particle respectively powder characteristics.

It will be discussed how the process parameters influence particle characteristics, such as size distribution, microstructure, morphology, and crystallinity which are important for the generation of functional nanomaterials.

2.2 Influence of Pulsed Precursor Delivery on Particle Size and Size Distribution

Pulsed flows in reactors are so far mostly known for processes in the liquid and less for the gas phase. Pulsed plasmas were used to generate FePt nanoparticles from the gas phase [5]. Pulsed reactant flows are used in Atomic Layer Deposition (ALD [6]). A pulsed flow of liquid reactants was used to produce carbon fibers in a continuous process [7]. For the liquid phase it could be shown that the particle size distribution (PSD) for droplets in an oscillating reactor becomes narrower [8]. Nanoparticles of very narrow size distribution can be generated in segmented liquid flows [9, 10].

In case of CVS a pulsed flow of reactants—depending on pulse length and frequency—can lead to a reduction in reactant and particle concentration by axial dispersion and thereby suppress dynamically the particle growth by chemical

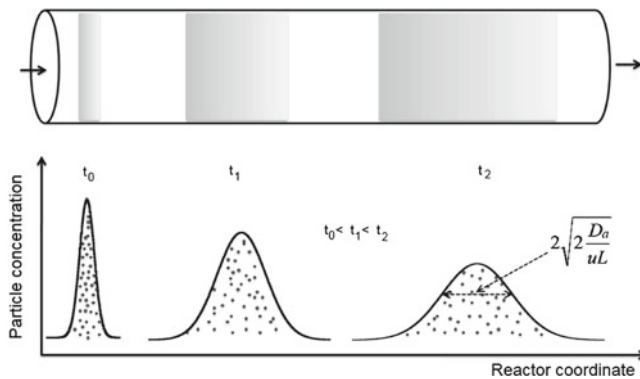


Fig. 2.2 The spreading of a precursor pulse according to the axial dispersion model (after Levenspiel [12])

reaction and coagulation during their residence time. In this way, the microstructure of the particles (degree and type of agglomeration and consequently PSD) can be influenced. A pulsed flow of reactants can be implemented experimentally using a laser flash evaporator [11] by pulsing the CO_2 -laser power. It is of great advantage for a systematic investigation that all other process parameters remain unchanged. In this way, it should be possible to reduce the particle number density and to achieve narrow PSD in CVS. Figure 2.2 schematically illustrates this idea. When the pulse of precursor is delivered into the reactor (time: t_0) due to the molecular diffusion it starts to spread (times: t_1 and t_2) along the reactor. This can be described by using the axial dispersion coefficient, D_a [12]:

$$\frac{\partial C}{\partial t} = \left(\frac{D_a}{uL} \right) \frac{\partial^2 C}{\partial z^2} - \frac{\partial C}{\partial z} \quad (2.1)$$

where (D_a/uL) is the parameter measuring the extent of the axial dispersion and is called ‘dispersion number’ (dimensionless, the inverse of the Bodenstein number, Bo [13]), u is the velocity, L is the reactor length, C is the concentration, and $z = (ut + x)$. The solution of Eq. (2.1) is a symmetrical curve similar to a Gaussian distribution described by mean value and variance ($\sigma^2 = 2D_a/uL$). The main challenge is to keep pulses apart from each other in order to avoid their intermixing and to retain a pulsed flow for the total residence time. As discussed later, this will be achieved by varying the laser pulse repetition frequency and duty cycle.

2.2.1 Experimental Methodology

Particle synthesis. Figure 2.3 shows a schematic drawing of the CVS setup used for the TiO_2 particle synthesis from titanium diisopropoxide bis (tetramethylheptan

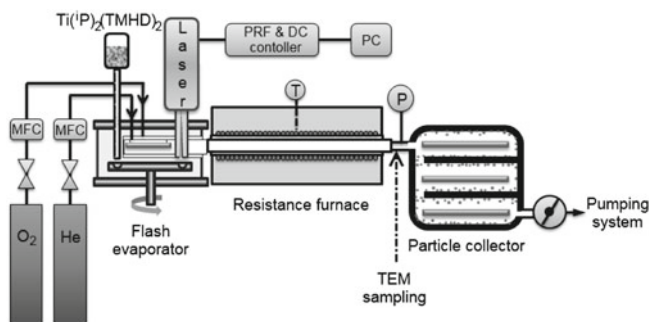


Fig. 2.3 The CVS setup for synthesis of TiO₂ nanoparticles using laser flash evaporation as precursor delivery method

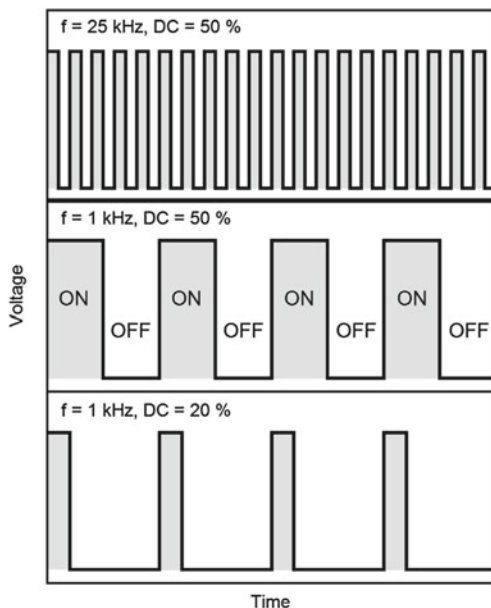
edionate), Ti(ⁱP)₂(TMHD)₂ (95 %, ABCR, Germany). The solid precursor was continuously (manually) fed into the flash evaporator and evaporated using a CO₂ laser (Coherent GEM, operated at 95 W). After the precursor is evaporated, its vapor was carried by a helium stream (1,020 sccm) into the hot-wall reactor where the TiO₂ particles are formed in reaction with 1,000 sccm of oxygen at a temperature of 1,273 K and a pressure of 20 mbar. Particles are collected in the thermophoretic particle collector.

In order to study the influence of the particle number concentration on the width of the PSD, precursor has to be delivered in pulses to the reactor. This was utilized by changing the CO₂ laser pulse repetition frequency and the duty cycle. Each state when the laser is “ON” defines the amount of the precursor in the reactor and consequently the particle number concentration. In the experiments, the laser repetition frequency and duty cycle were varied ($f = 0.05\text{--}25\text{ kHz}$; $\text{DC} = 20\text{--}100\%$). A schematic illustration of some frequency and duty cycle combinations are shown in Fig. 2.4. When the laser is operated at a frequency of 25 kHz or duty cycle of 100 %, precursor delivery can be considered as continuous.

Particle characterization. Crystal structure and phase composition of the as synthesized powders were analyzed from the X-ray diffraction (XRD) patterns obtained using the Panalytical X’Pert Pro powder diffractometer. The XRD patterns were refined by the Rietveld method using the MAUD software [14]. The XRD patterns were recorded using CuK_α radiation in an 2θ interval from $20\text{--}120^\circ$ with steps of 0.03° and counting time 200 s/step.

Transmission electron microscopy (TEM) was used to determine the particle size and size distribution of TiO₂ nanoparticles. For this purpose thermophoretic (in-situ) particle deposition on Cu grids with carbon film was used. Images were recorded using a Philips Tecnai TEM-F20 Super Twin operating at 200 kV (0.23 nm point resolution) with a Gatan Multiscan CCD (794IF) camera. The PSD was obtained by the log-normal size distribution (fit using the geometric mean as particle size and the geometric standard deviation, σ_g , to describe the width of the distribution) of

Fig. 2.4 Schematic illustration of some frequency and duty cycle combinations used (the gray areas represent the 'ON' state of the laser in which a defined amount of precursor is evaporated)



binned data obtained from the TEM images by measuring the size of several hundred particles.

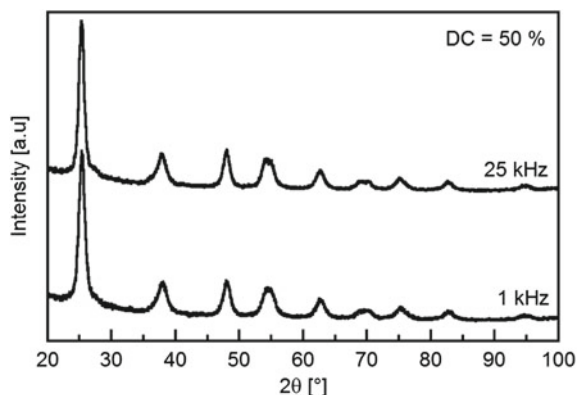
In order to determine the degree of particle agglomeration, photon correlation spectroscopy (PCS) was used to measure the particle size by a Zetasizer Nano S (Malvern) equipped with a green laser ($\lambda = 532 \text{ nm}$). Prior to the measurement 12.5 mg nanoparticles were dispersed in 25 ml of 0.01 M HCl ($\text{pH} \approx 2$) and ultrasonically treated.

2.2.2 Results and Discussion

Figure 2.5 shows diffraction patterns of two selected powders synthesized by evaporating the precursor using a CO_2 laser operated at higher (25 kHz) and lower (1 kHz) frequencies. The as-synthesized TiO_2 powders are highly crystalline nanoparticles consisting of anatase with a very small contribution of rutile.

The powders synthesized varying the laser duty cycle ($\text{DC} = 20\text{--}100 \%$) showed high crystallinity as well. It is interesting to mention that only powders synthesized by evaporating the precursor with the laser operating at 25 kHz and 50 % of duty cycle were grayish, while all other powders were white, clearly indicating a difference in the precursor concentration in the reactor. At high frequency (25 kHz), due to the high precursor concentration, the process conditions were not optimal for complete precursor decomposition.

Fig. 2.5 XRD patterns of TiO_2 particles synthesized using a CO_2 laser operating at 50 % of duty cycle and two frequencies: 1 and 25 kHz (as an example)



2.2.2.1 Influence of Laser Pulse Repetition Frequency

For lower laser pulse repetition frequencies it is expected that the particle number concentration in the reactor is lower and thus the formation of smaller particles with a narrower PSD was expected. Figure 2.6 shows TEM images of TiO_2 particles synthesized using a high (25 kHz) and a low (0.05 kHz) laser frequency. From the images it can be already seen that the particle size does not differ much. Detailed analysis of particle size from the TEM images for the frequency range 0.05–25 kHz showed that the particle size is not affected by a change of the laser pulse repetition frequency (Fig. 2.7). The slight fluctuation in particle size observed at lower frequency is most likely related to a variation of the amount of precursor available for evaporation due to the manual feed of the precursor powder. Although it was expected that with lowering the laser pulse repetition frequency, the PSD will become narrower, only an insignificant narrowing of the PSD from σ_g of 1.25(3) at 25 kHz to 1.23(2) at 0.05 kHz was observed (Fig. 2.8).

Friedlander [15] has shown that the PSD can reach a limiting ‘self-preserving’ size distribution. The self-preserved size distribution is characterized by a geometric standard deviation of 1.40 and 1.46 for the continuum and free molecule regime, respectively. As the width of TiO_2 PSD presented here is about 1.25, the self-preserved size distribution has not been reached and is already rather narrow. Therefore, variations in other process parameters mask probably changes in the size distribution originating from the pulsed operation of the flash evaporator.

Kodas and Friedlander [16] investigated the monodisperse aerosol production in tubular flow reactors and found that in order to produce monodisperse aerosols, nucleation and growth should be separated, the residence time distribution should be narrow and particles should be exposed to a similar monomer concentration. Therefore, the manual precursor feeding, which causes the fluctuations in the evaporated amount of precursor, could be one reason for the insignificant change in the width of the PSD.

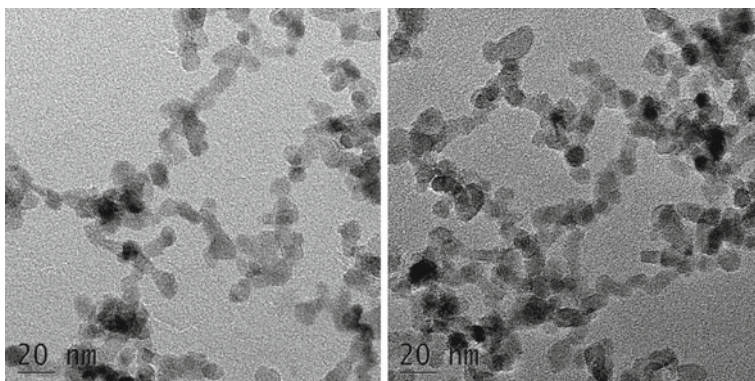


Fig. 2.6 TEM images of TiO₂ nanoparticles synthesized using a laser operating at 25 kHz (*left*) and 0.05 kHz (*right*) with 50 % of duty cycle

Fig. 2.7 Particle size as a function of laser pulse repetition frequency at 50 % duty cycle obtained by the TEM image analysis

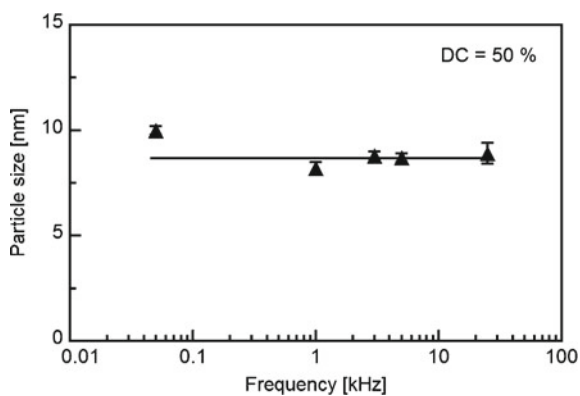
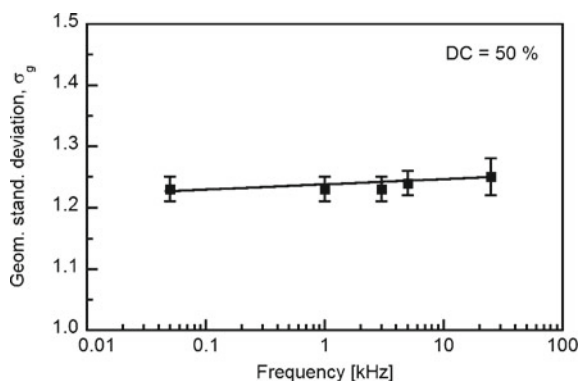


Fig. 2.8 Geometric standard deviation as a function of laser pulse repetition frequency at 50 % duty cycle obtained by the TEM image analysis



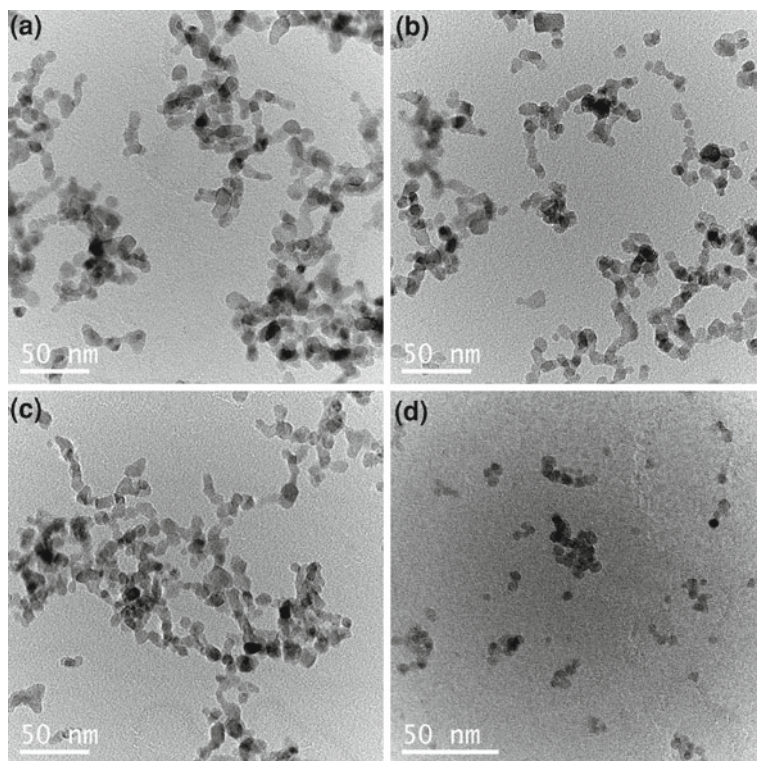


Fig. 2.9 TEM images of TiO_2 nanoparticles synthesized using the laser operating at 1 kHz and different duty cycles: 100 (a), 80 (b), 60 (c), and 20 % (d)

2.2.2.2 Influence of Laser Duty Cycle

Figure 2.9 shows the TEM images of TiO_2 particles synthesized using a frequency of 1 kHz and varying the duty cycles. It is clear that the duty cycle has a significant influence on the particle size, as it is also observed in Fig. 2.10. Therefore, choosing a lower duty cycle, the amount of precursor, and consequently the number concentration of particles was evidently reduced, leading to the formation of smaller particles.

Not only the particles size decreased but also the degree of agglomeration showed a significant decrease, as it can be seen from the cubed ratio of particle size obtained from the PCS and XRD (Fig. 2.11). Concerning the width of the PSD, results showed that at 1 kHz, the duty cycle has no influence on the PSD (Fig. 2.12). Similar conclusions can be drawn for the experiments performed at lower frequency (0.2 kHz), shown in Figs. 2.13, 2.14, and 2.15. The duty cycle had only an impact on the particle size (Figs. 2.13, 2.14), while no influence on the width of the PSD was observed (Fig. 2.15).

Fig. 2.10 Particle size obtained from the TEM images as a function of laser duty cycle at 1 kHz

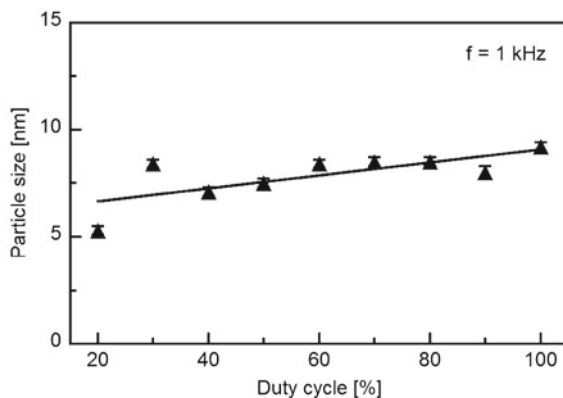


Fig. 2.11 Degree of agglomeration (cubed ratio of particle size obtained from the PCS and XRD) as a function of duty cycle at frequency of 1 kHz (line is only a guide to the eyes)

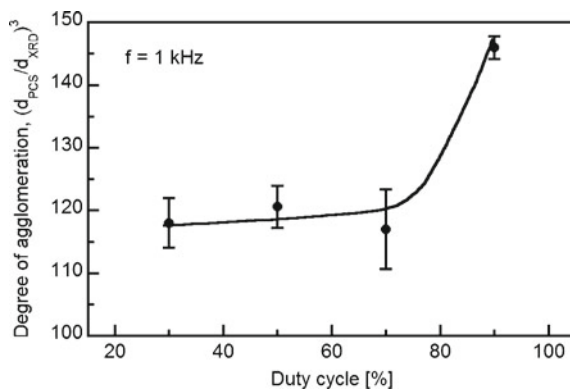
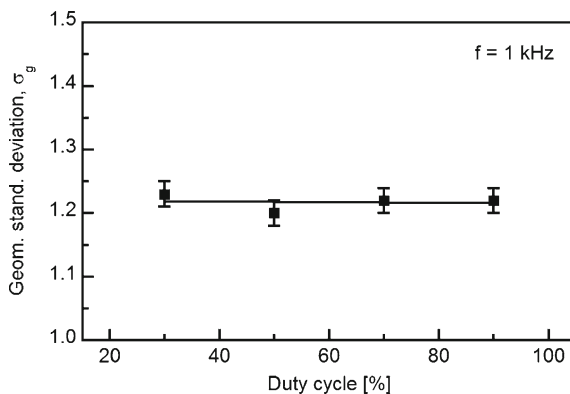


Fig. 2.12 Geometric standard deviation (obtained from the log-normal fit of the TEM data) as a function of the laser duty cycle at 1 kHz



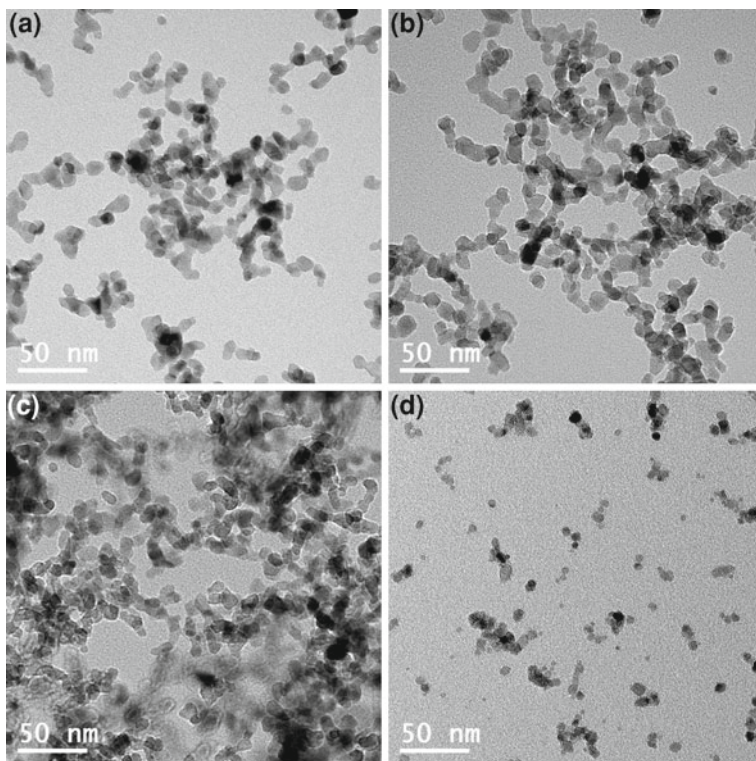


Fig. 2.13 TEM images of TiO₂ nanoparticles synthesized using the laser operating at 0.2 kHz and different duty cycles: 100 (a), 80 (b), 60 (c), and 20 % (d)

Fig. 2.14 Particle size (obtained from the TEM images) as a function of laser duty cycle at 0.2 kHz

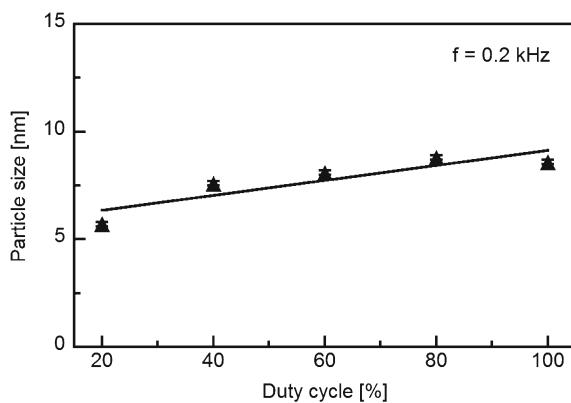
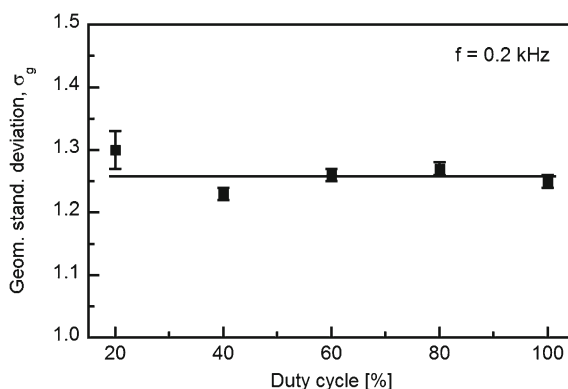


Fig. 2.15 Geometric standard deviation (obtained from the log-normal fit of the TEM data) as a function of laser duty cycle at 0.2 kHz



2.3 Influence of the Time-Temperature Profiles on Powder Characteristics

The quality and application of nanostructured materials are strongly related to the particle and powder characteristics. Powders of small grain size, narrow size distribution, low degree of agglomeration, and high purity are required for the fabrication of solid nanocrystalline materials and the exploitation of size effect in applications. A large variety of methods [17] based on solid, liquid, or gas phase processes are in use for nanocrystalline powder synthesis. For the production of nanocrystalline materials from nanopowders produced by gas phase methods not only the grain size, but also the particle size, i.e. the control of the particle morphology or agglomeration, is important [18]. The objective in most nanoparticle synthesis is to grow dense, non-agglomerated nanoparticles. Therefore, it is requisite to understand the process of particle formation in order to have control upon the powder characteristics.

In the following a simple reaction-coagulation-sintering model (CVSSIN) [4] is used to describe the CVS process. As a model system titania (TiO_2) was used. Nanocrystalline titania, especially anatase, is used in applications such as photocatalysis and photovoltaics [19, 20], thus substantial experimental and theoretical information are available. Additionally, the product of the process is in all relevant cases crystalline, consisting mostly of anatase. This enables not only a detailed model description of the CVS process, but also an extensive characterization of the generated particles and the product powders. The model assumes stationary, ideal, 1D plug flow, without axial dispersion. Processes, which influence the formation of particles from molecular precursors and powder characteristics, such as particle microstructure, morphology, size distribution, and crystallinity are included in the model: conversion of the precursor into monomers (growth species), formation of clusters (primary particles or grains) from monomers, coagulation of primary particles and formation of agglomerates, sintering of the primary particles within the agglomerates, heat exchange (with the hot wall), and heat production by the above processes. In this study, we demonstrate the influence of the key CVS-process

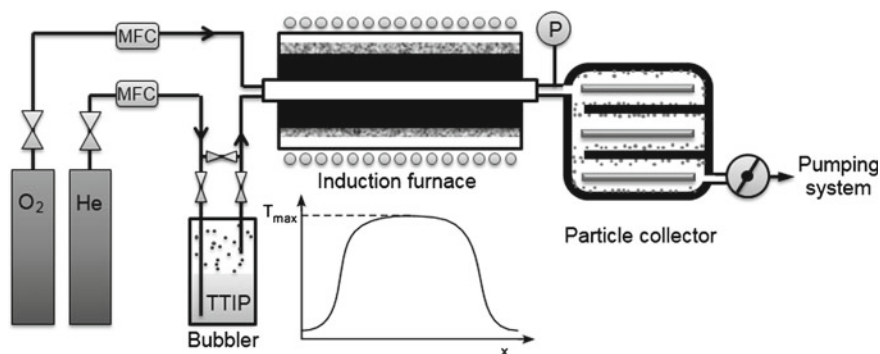


Fig. 2.16 The CVS setup used for the synthesis of TiO₂ nanoparticles

parameter, the time-temperature profile in the CVS-reactor, on the particle generation and the corresponding powder characteristics, especially the degree of agglomeration.

2.3.1 Experimental Methodology

Powder synthesis. Figure 2.16 shows a schematic illustration of the CVS setup used for the synthesis of TiO₂ particles from titanium-tetraisopropoxide, TTIP (98 %, ABCR, Germany). It consists of a precursor delivery system (bubbler), a hot-wall reactor with an alumina tube, a thermophoretic powder collector, and a pumping system (Busch Cobra NC 0600A). Helium carrier gas (150 sccm) is used to transport the precursor vapor from the bubbler (the temperature is maintained at 333 K using an oil thermostat) to the reaction zone, and oxygen (1,000 sccm) is used as a reactant. The mass flow of the gases is controlled by thermal mass flow controllers (MKS Instruments). In the hot zone of the reactor the precursor vapor decomposes and reacts to form oxide particles. The particles are then transported by the gas stream to the particle collector, where they are separated from the carrier gas flow and byproducts by thermophoresis. A hot-wall reactor is assembled using an induction furnace. The reactor tube (alumina) was inductively heated using a graphite susceptor and a high frequency generator (Hüttlinger BIG 20/100). Reactor wall temperatures from 873 up to 2,023 K are investigated and measured using a pyrometer (Sensotherm Metis MI16, $\lambda = 1.6 \mu\text{m}$). The process pressure is held constant at 20 mbar for all experiments using a capacitive absolute pressure gauge (MKS Baratron) and a butterfly valve with adjusting the effective pumping speed of the vacuum pump at the reactor exit.

Powder characterization. Powders have been characterized using X-ray diffraction photon correlation spectroscopy and high-resolution transmission microscopy as described in Sect. 2.2.1.

Fig. 2.17 Gas temperature profiles (full lines) as a function of reactor coordinate for hypothetical ‘flat’ wall temperature profiles (dashed lines)

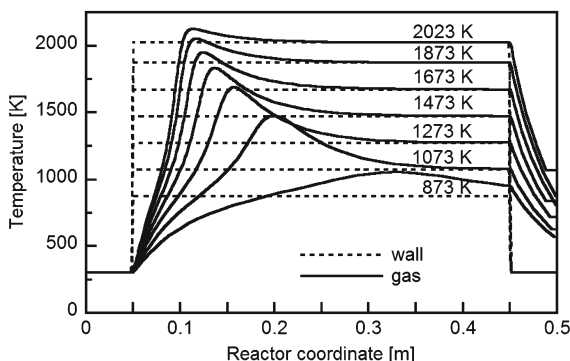
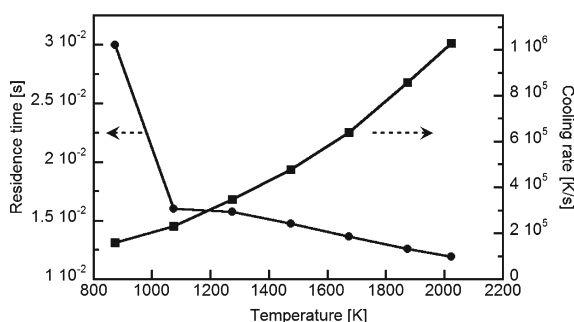


Fig. 2.18 Residence time and maximum cooling rate in the CVS reactor as a function of the maximum wall temperature obtained from the model



2.3.2 Results and Discussion

Results of the CVSSIN model. The CVSSIN model revealed that a simple increase of the wall temperature not only increases the gas temperature in the reactor, but changes the time-temperature profile completely (Fig. 2.17). As the conversion of the TTIP precursor into TiO_2 particles is a highly exothermic reaction, a hot spot in the reactor develops. The difference between the maximum gas temperature and the wall temperature decreases with increasing wall temperature and the position of the hot spot moves closer to the reactor entrance. The total residence time in the reactor decreases and the cooling rate at the exit of the reactor increases with increasing wall temperature (Fig. 2.18). As the temperature increases the primary and agglomerate particle size increases (Fig. 2.19). The agglomerate size reaches a maximum at 1,273 K (Fig. 2.19). Above these temperatures, due to a faster chemical reaction rate, the number density of smaller particles increases, and sintering is enhanced, leading to a decrease of agglomerate size.

The degree of agglomeration (cubed ratio of agglomerate and primary particle size) displays a minimum after a first maximum which is formed due to the particle nucleation burst by chemical reaction (Fig. 2.20). At that minimum the gas temperatures are sufficiently high to completely coalesce the very small primary particles

Fig. 2.19 Primary and agglomerate size obtained from the model as a function of the maximum wall temperature

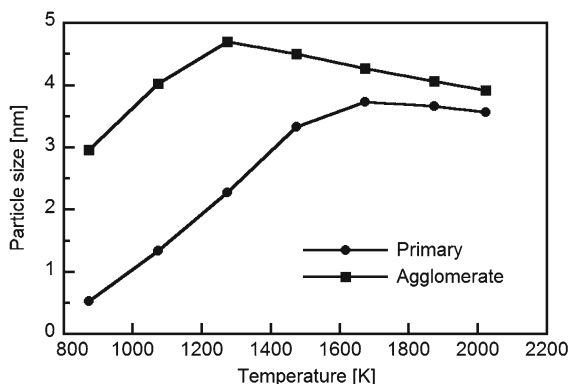
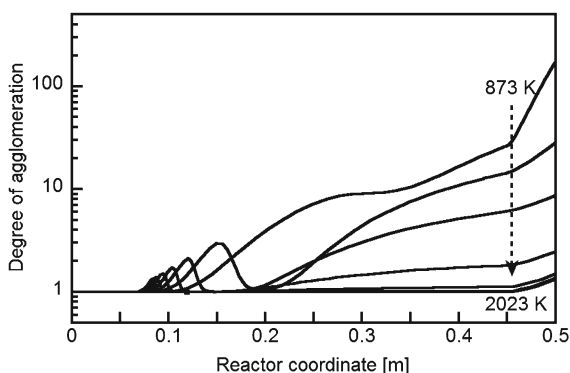


Fig. 2.20 Degree of agglomeration obtained from the model as a function of reactor coordinate



inside of the agglomerates. However, at the reactor exit, where the particles are collected, agglomeration increases and shows a maximum for particles produced at 873 K (Fig. 2.20). At the lowest process temperature the sintering kinetic of the primary particles is too slow, while at higher process temperatures the sintering kinetics is enhanced and coalescence is possible, leading to a reduction of the agglomeration (Fig. 2.21).

Experimental results. Figure 2.22 displays a typical X-ray diffraction pattern of a TiO_2 powder synthesized at 1,273 K together with the Rietveld refinement. The XRD patterns of all as-synthesized TiO_2 powders [21] show strong reflections of the anatase phase indicating that the powders are well crystalline. The Rietveld analysis of the XRD data shows very good agreement between experiment and refinement. The TEM image of TiO_2 particles synthesized at 1,273 K (Fig. 2.23a) shows that particles are spherical with a size of about 7 nm (Fig. 2.23b). The crystallite size obtained from Rietveld refinement of the XRD data (volume weighted) and particle size obtained from the PCS (volume weighted) as a function of process temperature are shown in Fig. 2.24. The crystallite size (as a measure for the primary particle size) increases with process temperature, and ranges from about 2 nm at 873 K up

Fig. 2.21 Degree of agglomeration as a function of maximum wall temperature according to the CVSSIN model

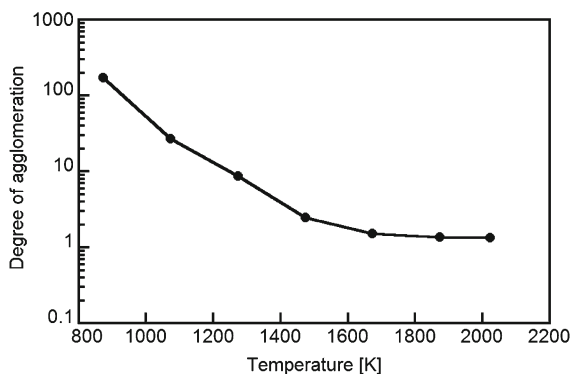
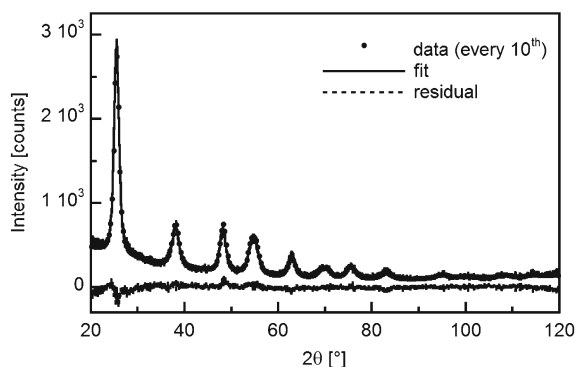


Fig. 2.22 The XRD pattern of TiO_2 nanoparticles synthesized at 1,273 K using Rietveld refinement



to 11 nm at 2,023 K, while the agglomerate size (as measured by PCS) decreases. The cubed ratio of the particle size determined from PCS to the primary particle size obtained from XRD is a measure for the degree of agglomeration and it is shown in Fig. 2.25. The experimental data follows the trend of the CVSSIN model showing that at the highest process temperature (2,023 K) the lowest degree of agglomeration is achieved as it was predicted by CVSSIN model.

However, the absolute values of the model are considerably smaller than the experimentally determined data. It is known [22] that surface reactions dominate particle growth at lower temperatures.

As surface reactions were not included in the CVSSIN model, this could be the reason for the observed discrepancy between model and experimental results at lower temperatures. On the other hand, the preparation of colloidal particle dispersions (ultrasonic treatment in water, no surfactant added) and the measurement of the agglomerate size by PCS may not be the optimum procedure to compare experimental with simulational results. It was shown by Grass et al. [23] that non-agglomerated particles can be formed at low precursor flow rates and high quenching rates. Materials properties (solid state diffusion coefficients) and the time-temperature profile

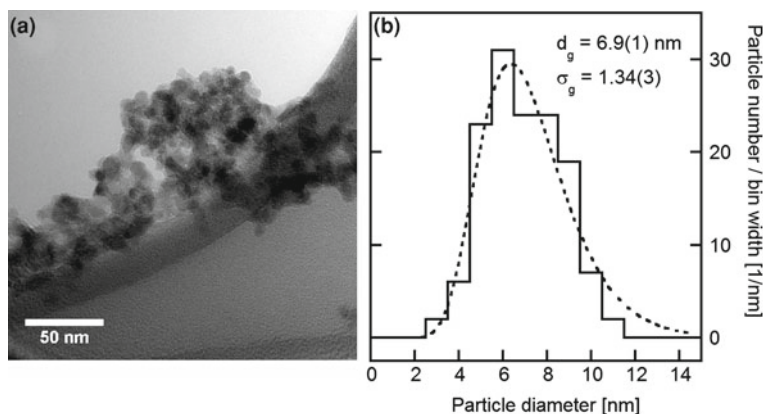
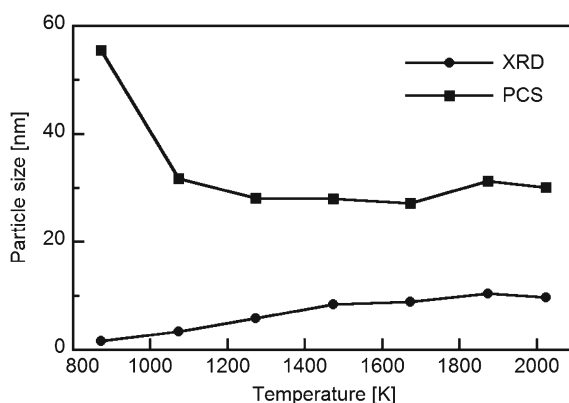


Fig. 2.23 TEM image (a) and corresponding PSD (b) of TiO_2 nanoparticles synthesized at 1,273 K

Fig. 2.24 Particle size obtained from XRD and PCS (volume weighted) as a function of process temperature (error bars are smaller than symbols)

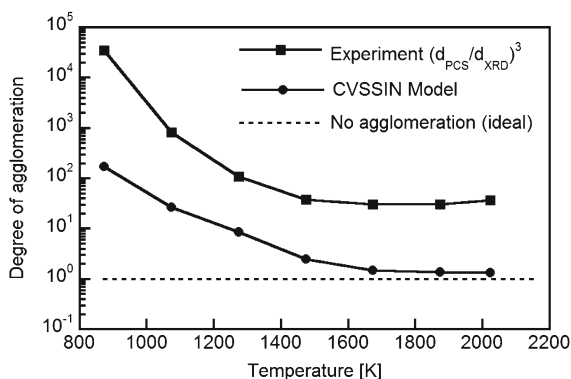


control the agglomeration. This is in agreement with the results of titania generated by CVS presented here.

2.4 Control of Composition by Laser Flash Evaporation: Crystal and Local Structure of Cobalt Doped Zinc Oxide Nanoparticles

Nanostructured magnetic semiconductor materials are promising materials for novel concepts in information technology. Inspired by theoretical predictions, at first by Dietl [24] later by Sato and Katayama-Yoshida [25], extensive research efforts have been carried out by many groups on searching for room temperature ferromagnetism

Fig. 2.25 Comparison of the experimentally determined degree of agglomeration (calculated from the particle size obtained from PCS and XRD) with the CVSSIN model



in transition metal (TM) doped ZnO. The key requirement for practical applications is the generation of intrinsic ferromagnetism with Curie temperatures above room temperature. The coupling between magnetism and charge carriers is possible, if the magnetic dopants are located on (substitutional) lattice sites. As chemical composition, crystal and local structure play an important role in the particle properties, a detailed structural characterization is essential for their understanding. Therefore, the crystal and local structure of the Co-doped ZnO, $Zn_{1-x}Co_xO$ ($x = 0.25, 0.30$, and 0.50) were studied in detail.

2.4.1 Experimental Methodology

Particle synthesis. Nanocrystalline Co-doped ZnO particles ($Zn_{1-x}Co_xO$, $x = 0.25, 0.30$, and 0.50) are synthesized in the CVS reactor which consists of two sequential resistive furnaces and a ceramic (alumina) tube (Fig. 2.26). Anhydrous solid zinc acetate, $Zn(OAc)_2$ (Sigma Aldrich, 99.9% purity), and cobalt acetate, $Co(OAc)_2$ (Sigma Aldrich, 99.9% purity), powders are thoroughly mixed in a mortar under inert conditions inside a glovebox corresponding to a nominal Co content, x . The precursor mixture was transferred under inert conditions to the laser flash evaporator. The radiation of a CO_2 laser (95 W, $f = 25$ kHz, DC = 50 %) is used to evaporate the precursor mixture. The precursor vapors are transported into the hot-wall reactor using helium (1,020 sccm) as carrier gas where they react with oxygen (1,000 sccm) to form particles.

A hot-wall temperature of 1,373 K and a total pressure of 20 mbar are used for all experiments. The particles are thermophoretically separated from the gas flow in a particle collector.

Particle characterization. Atomic absorption spectroscopy (AAS) is used to determine the Co concentration in Co-doped ZnO nanoparticles. The measurement was carried out using a Thermo Scientific Atomic Absorption Spectrometer (M Series).

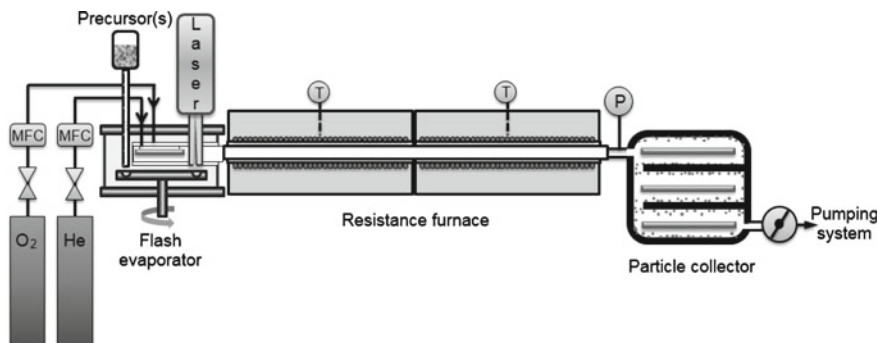


Fig. 2.26 The CVS setup for the synthesis of Co-doped ZnO nanoparticles from mixtures of precursor powders by laser flash evaporation

Fourier transform infrared (FTIR) spectroscopy was used to compare absorption lines of the precursors with the emission line of the CO_2 laser used for their evaporation. Measurements were performed on a Bruker IFS 66v/s instrument.

As described in Sect. 2.2.1 XRD measurements were used in order to analyze the phase composition, crystal, and microstructure of the samples.

In order to investigate the local structure around Zn and Co atoms in Co-doped ZnO nanoparticles, X-ray absorption spectra (XAS) were measured at the Co K -edge and Zn K -edge at the HASLAB (DESY) beamline X1. The absorption of the samples is optimized by diluting appropriate amounts homogeneously into starch powder and pressing a pellet (13 mm diameter) uniaxially (25 kN/10 min). Transmission spectra are collected at ambient temperature. The spectra of commercial CoO and Co_3O_4 powders (Sigma Aldrich) are also recorded as a reference. The X-ray absorption fine structure (XAFS) data were reduced using the program *xafsX* [26]. The extracted extended X-ray absorption fine structure (EXAFS) data are then analyzed by the Reverse Monte Carlo method (RMC) using the *rmcxas* program [27]. Initial atomic configurations are generated from results of the Rietveld refinements of XRD data of the corresponding samples and contain an appropriate number of Co atoms. Zn and Co EXAFS spectra for $x = 0.25$ and 0.30 are analyzed simultaneously using a single atomic configuration, where an appropriate number of Zn atoms in a wurtzite lattice are substitutionally replaced by Co atoms. The sample with $x = 0.5$ was analyzed assuming a mixture of CoO (67 vol %) and Co_3O_4 (33 vol%) consistent with the XRD analysis as initial configurations. Theoretical amplitude and phase functions for RMC analysis are obtained using the program *FEFF* (version 8) [28].

Fig. 2.27 Correlation between actual (x_a) and nominal (x) Co content (error bars are smaller than the symbols) [29]

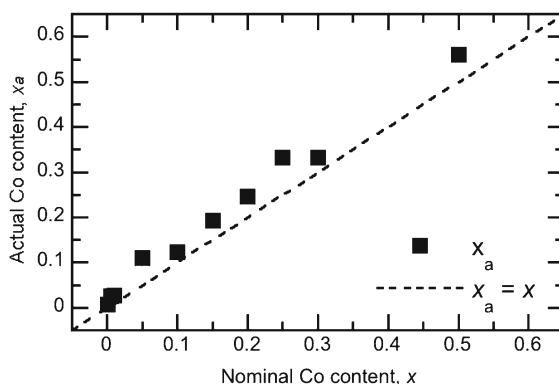
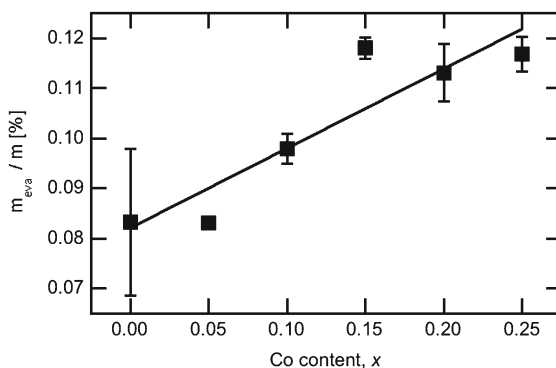


Fig. 2.28 Evaporated mass fraction of the precursor mixture as a function of nominal Co content [29]



2.4.2 Results and Discussion

Chemical composition. As shown in a previous study [29] the actual Co concentration (x_a) in the as-synthesized $\text{Zn}_{1-x}\text{Co}_x\text{O}$ nanoparticles is systematically higher compared to the nominal concentration (x) of the precursor mixture used (Fig. 2.27). It is also observed that the evaporation rate of the precursor mixture as determined from its weight loss is enhanced with increasing Co concentration (Fig. 2.28) which may explain the systematic deviation of the actual Co content from the nominal. The increasing evaporation rate of the precursor mixture with increasing Co content can be explained by the higher absorption of laser light by Co-acetate compared to Zn-acetate as can be seen from a comparison of the FTIR spectra of the precursors with the laser emission line (Fig. 2.29). However, the chemical composition of the product can be easily adjusted knowing the evaporation rates of the used precursor materials. This is of great advantage for the generation of complex oxide materials.

Fig. 2.29 FTIR spectra of the Zn- and Co-acetate precursors and the emission line of the CO₂ laser (wavelength of 10.6 μm) [29]

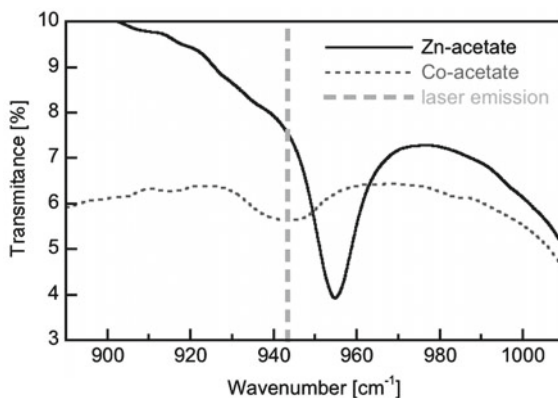


Fig. 2.30 Rietveld refinement of X-ray diffractograms of as-synthesized $\text{Zn}_{1-x}\text{Co}_x\text{O}$ nanoparticles with nominal Co contents of $x = 0.25, 0.30$, and 0.50 (vertical bars correspond to the three most pronounced Bragg reflections for wurtzite ZnO, CoO, and Co_3O_4) refinement results are compiled in Table 2.1

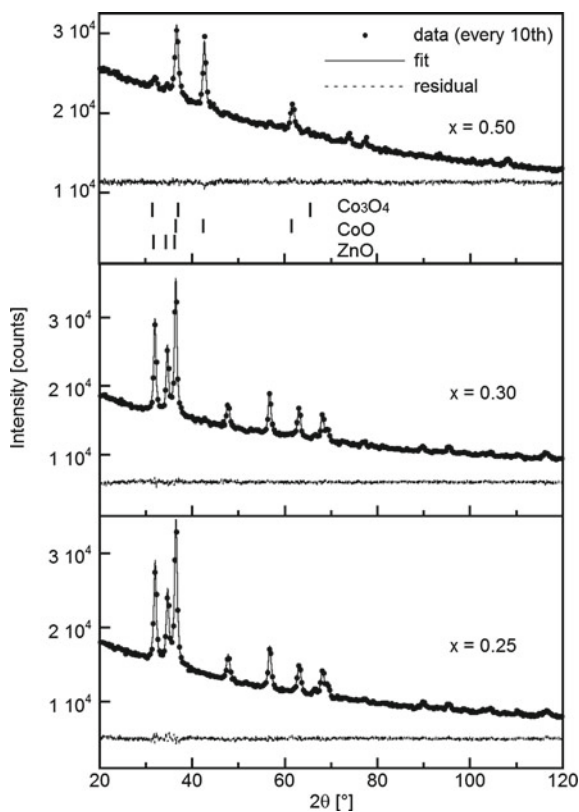
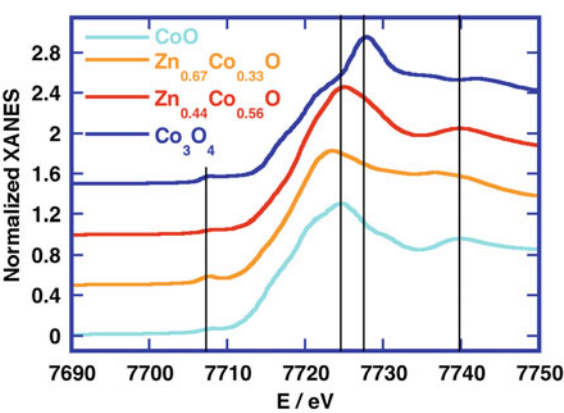


Table 2.1 Results of Rietveld refinement of the XRD data of $\text{Zn}_{1-x}\text{Co}_x\text{O}$ nanoparticles ($x = 0.25, 0.30$, and 0.50)

Nominal Co content x	Actual Co content x_a	Phase composition (vol%)			ZnO (wurtzite)		
		ZnO	CoO	Co ₃ O ₄	Lattice parameters		Crystallite size
		<i>P63mc</i>	<i>Fm-3m</i>	<i>Fd-3m</i>	<i>a</i> (Å)	<i>c</i> (Å)	
0.25	0.30	100	–	–	3.2584(2)	5.2121(4)	20.0(1)
0.30	0.33	97.5	2.5(3)	–	3.2572(2)	5.2098(4)	23.2(1)
0.50	0.56	25	52(2)	23(2)	3.259(1)	5.214(3)	14.3(5)

Fig. 2.31 Co *K*-edge XANES spectra of $\text{Zn}_{1-x}\text{Co}_x\text{O}$, CoO, and Co_3O_4 the actual Co contents are indicated as obtained by chemical analysis



Crystal structure. Figure 2.30 displays the XRD patterns and the result of the Rietveld refinement for as-synthesized $\text{Zn}_{1-x}\text{Co}_x\text{O}$ nanoparticles ($x = 0.25, 0.30$, and 0.50). The Rietveld refinement of the XRD data shows that the sample with $x = 0.25$ consists purely of wurtzite phase. In samples with a Co concentration of $x \geq 0.30$, CoO, and Co_3O_4 are present as additional phases. The maximum Co solubility in wurtzite-type ZnO, for which the particles are still single-phase, varies greatly for samples of the same nominal composition but prepared by different methods [30–34]. The Co solubility limit in nanoparticles studied in this work, is about $x_a = 0.33$ (nominal content $x = 0.25$) (Fig. 2.30, Table 2.1).

Further Co addition causes the generation of second phases: CoO in the sample with nominal Co content of $x = 0.30$ ($x_a = 0.332$) and CoO and Co_3O_4 in the sample with $x = 0.50$ ($x_a = 0.56$). This is consistent with other literature reports [35, 36].

Local structure. XAFS provides information about the distribution and location of Co in the wurtzite lattice complementary to X-ray diffraction. Figure 2.31 shows normalized Co *K*-edge XANES spectra of the $\text{Zn}_{1-x}\text{Co}_x\text{O}$ ($x = 0.25$ and 0.50) together with reference spectra of CoO and Co_3O_4 . Comparing the XANES spectra of $\text{Zn}_{1-x}\text{Co}_x\text{O}$ with the spectra of the CoO reference, reveals that the Co is present

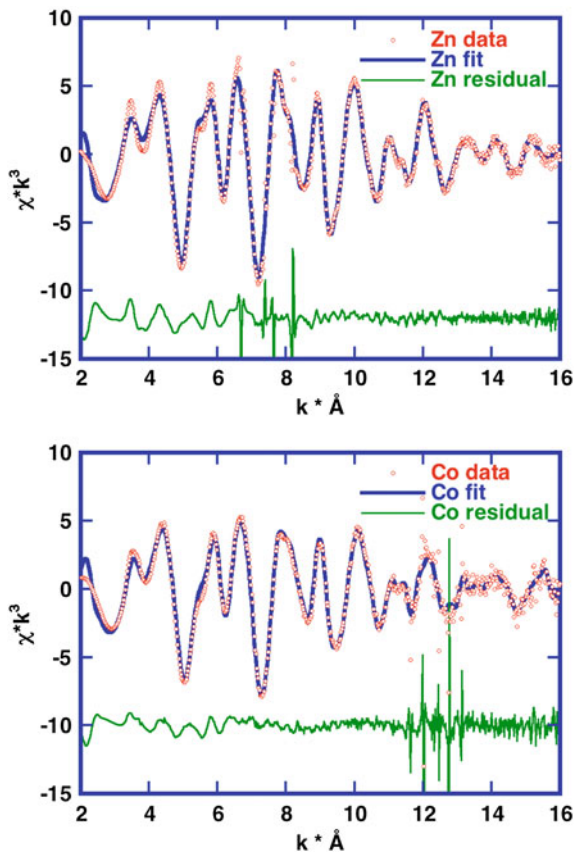


Fig. 2.32 Zn (*top*) and Co *K*-edge (*bottom*) EXAFS spectra for $\text{Zn}_{1-x}\text{Co}_x\text{O}$ $x = 0.25$ fit by Reverse Monte Carlo modeling. The *sharp peaks* in the spectra are due to monochromator glitches. For the initial atomic configuration substitutional Co atoms on Zn sites were assumed

in the Co^{2+} valence state. The small pre-edge peak at about 7,708 eV appears due to the transition of Co $1s$ electron to $4p-3d$ hybridized states in tetrahedral symmetry [37]. This indicates that Co is either located on Zn sites or tetrahedral interstitial sites.

The EXAFS spectra of $\text{Zn}_{1-x}\text{Co}_x\text{O}$ samples with $x = 0.25$ (Fig. 2.32) and $x = 0.30$ are very similar as well as the Zn and Co *K*-edge spectra of each of these samples in contrast to the sample with $x = 0.5$ (Fig. 2.33). This indicates that Co atoms in the samples with lower Co content are on Zn lattice sites, whereas for the highest content investigated, Co occupies sites with different local structure. This observation is consistent with the XRD results described above. Therefore, the samples with $x = 0.25$ and $x = 0.30$ were fit by RMC modeling using a wurtzite lattice with Zn atoms randomly substituted by Co, according to the composition, as initial configuration. The results of the simultaneously fit Zn- and Co- spectra are

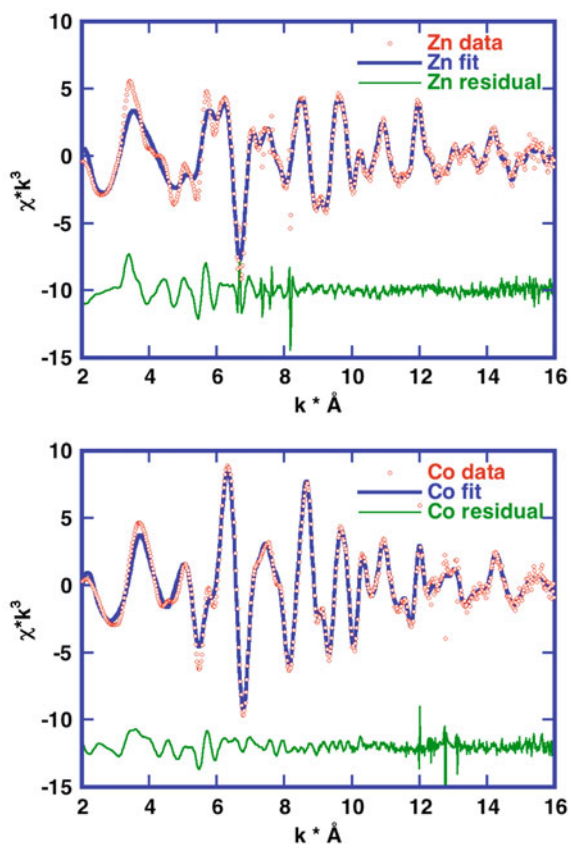
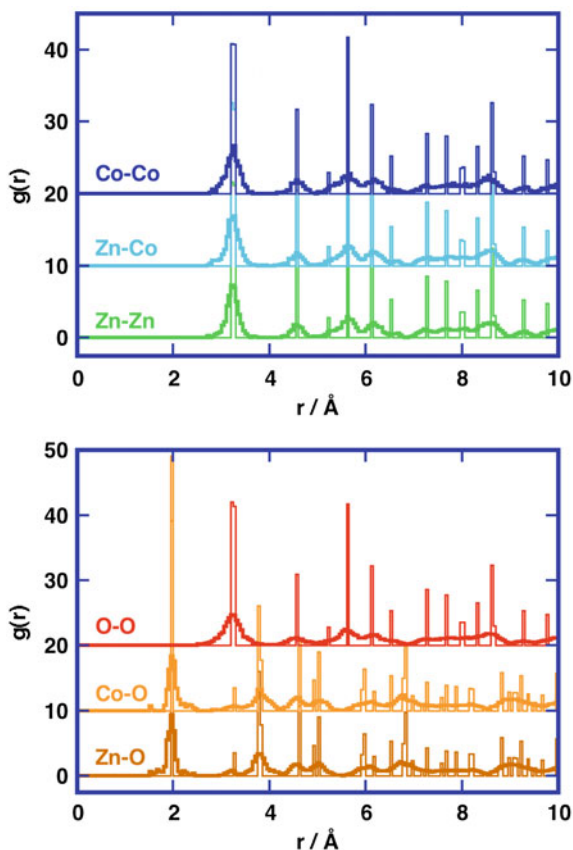


Fig. 2.33 Zn (*top*) and Co *K*-edge (*bottom*) EXAFS spectra for $\text{Zn}_{1-x}\text{Co}_x\text{O}$ $x = 0.5$ fit by Reverse Monte Carlo modeling. The *sharp peaks* in the spectra are due to monochromator glitches

shown in Fig. 2.32. The agreement between model and data is very good. The main deviations are due to monochromator glitches, insufficient background subtraction, and multiple scattering for which higher than pair correlation functions need to be considered. The corresponding partial pair distribution functions (PDFs) are shown in Fig. 2.34. All PDFs show essentially only a broadening of each peak due to thermal (and structural) disorder in the material.

In contrast to the samples with lower Co content the sample with $x = 0.5$ could not be fit well using a pure wurtzite model. Therefore, according to the XRD results the Co spectrum was fit with a mixture of CoO and Co_3O_4 and the Zn spectrum using pure ZnO in wurtzite structure (Fig. 2.34). The Co spectrum is fit quite well, whereas the fit of the Zn spectrum shows significant deviations from the data. Probably, Co is not segregated completely and is still present as dopant up to the solubility limit of about 33 mol% in the wurtzite lattice. This may also explain additional peaks in the

Fig. 2.34 Partial PDFs for $\text{Zn}_{1-x}\text{Co}_x\text{O}$ $x = 0.25$ derived from RMC. For the initial atomic configuration substitutional Co atoms on Zn sites were assumed. *Top* cationic partial PDFs, *bottom* anionic partial pair distribution functions (PDFs generated by the initial atom configuration: *thin lines*, PDFs of the RMC fit: *thick lines*)



Co-O (at 1.93 Å) and Co-Co (at 3.98 Å) PDF's of CoO (Fig. 2.35) and in the Zn-Zn PDF of the pure ZnO model for the Zn *K*-edge spectrum (Fig. 2.36).

The moment analysis of the partial PDFs (Table 2.2) shows that—within statistical error—the local structure samples with a lower Co content is identical. The phase separation visible in the XRD data at $x = 0.30$ could not be detected. The atom distances and the second moments which are a measure for the static and dynamic respectively structural and thermal disorder is identical for both samples of lower Co content as well as the second moment of the Co-Co, Zn-Co and Zn-Zn and the Co-O and Zn-O PDFs indicating that the majority of the Co atoms is on Zn lattice sites.

Fig. 2.35 Partial PDFs for $\text{Zn}_{1-x}\text{Co}_x\text{O}$ $x = 0.5$ derived from RMC simulation of the Co K -edge spectrum. A complete segregation of Co to a mixture of CoO (67 vol%) and Co_3O_4 (33 vol%) phases is assumed. *Top* partial PDFs for the CoO and *bottom* for the Co_3O_4 configuration (after the RMC fit: *thick lines*, initial configuration: *thin lines*)

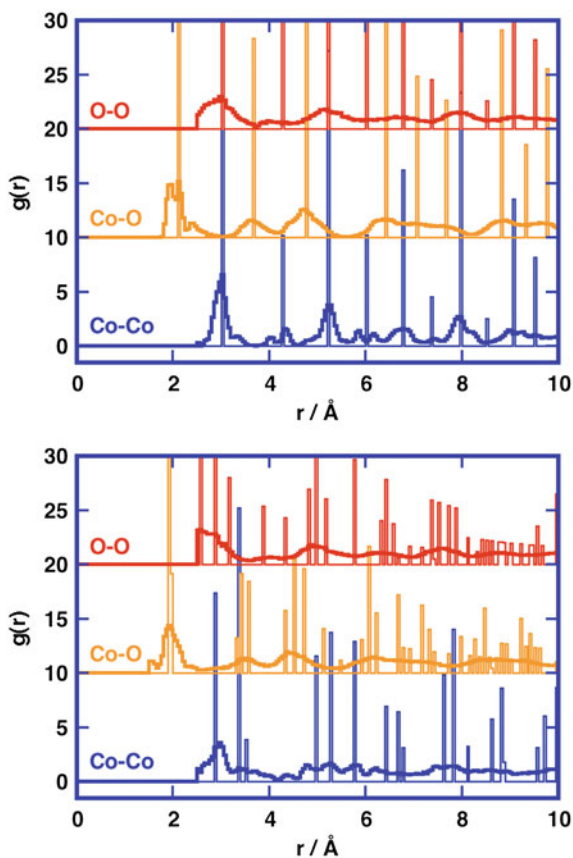


Fig. 2.36 Partial PDFs for $\text{Zn}_{1-x}\text{Co}_x\text{O}$ $x = 0.5$ derived from RMC. Partial PDFs obtained from the Zn K -edge spectrum using pure ZnO as model (after the RMC fit: *thick lines*, initial configuration: *thin lines*)

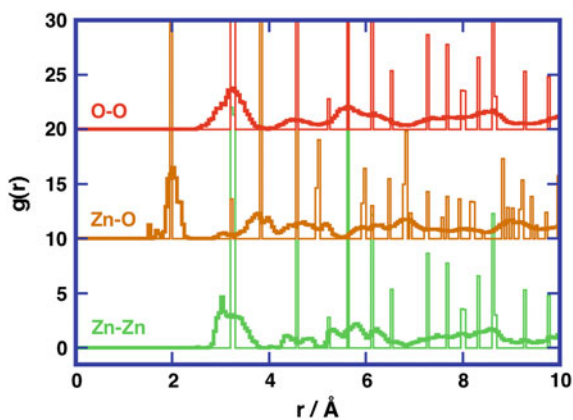


Table 2.2 Results of EXAFS data analysis of $\text{Zn}_{1-x}\text{Co}_x\text{O}$ nanoparticles using *rmcxas*

x (Co)	Shell	N	R (Å)	p_2 (10^{-3} Å^2)
0.25	Co-O	4.0(8)	2.02(3)	18(8)
	Co-Co	4.2(7)	3.23(3)	24(6)
	Co-Zn	na	3.23(3)	25(7)
	Zn-O	3.9(7)	1.96(3)	18(9)
	Zn-Co	4.2(7)	3.23(3)	24(6)
	Zn-Zn	7.6(12)	3.23(3)	20(7)
0.30	Co-O	3.9(8)	2.03(3)	17(8)
	Co-Co	4.2(7)	3.24(3)	27(7)
	Co-Zn	na	3.23(3)	25(8)
	Zn-O	3.9(7)	1.97(3)	14(7)
	Zn-Co	4.4(7)	3.23(3)	25(8)
	Zn-Zn	7.6(12)	3.22(3)	22(8)
0.50	(CoO)	Co-O	6.1(11)	51(17)
		Co-Co	12(2)	30(10)
	(Co ₃ O ₄)	Co-O	5.1(10)	33(12)
		Co-Co	6.9(17)	33(12)
	(ZnO)	Zn-O	3.9(8)	14(5)
		Zn-Zn	12(2)	50(11)

N the coordination number, R the interatomic distance, p_2 the second moment, *na* not analyzed

2.5 Summary and Conclusions

It has been shown that variations of precursor delivery and time-temperature profile in Chemical Vapor Synthesis have substantial influence on the particle and powder characteristics. The chemical engineering of CVS has been further developed, materials that can be produced by CVS have been extended to more complex systems and particles using a laser flash evaporator as precursor delivery method and powder characteristics have been optimized.

A novel method, pulsed precursor delivery using a laser flash evaporator, was developed to feed reactant material into a CVS reactor. A systematic study showed so far only limited influence on the width of the PSD, but a significant impact on the reduction of the particle size and the degree of agglomeration. The laser pulse repetition frequency had only little influence on the particle size and the size distribution. On the other hand, it is possible to lower the particle number concentration, thus to reduce the final particle size with rather narrow size distribution by decreasing the laser duty cycle. A low duty cycle leads also to a significant decrease in the degree of particle agglomeration.

The characteristics of nanocrystalline powders were studied using TiO_2 as a model material produced by chemical vapor synthesis. The time-temperature history of the gas phase in the reactor has considerable influence. With increasing wall temperatures the gas temperature becomes sufficiently high for a complete coalescence of the primary particles inside the agglomerates and the quenching rate at the reactor exit

fast enough to prevent extensive formation of hard agglomerates. Therefore, the fast quenching at the end of the reactor is essential for the formation of weakly agglomerated particles.

A high solubility of cobalt in ZnO is achieved using chemical vapor synthesis, as $\text{Zn}_{1-x}\text{Co}_x\text{O}$ nanoparticles for Co contents of up to $x_a = 0.33$ (according to chemical analysis) are of single wurtzite phase. Instrumental is here that the evaporation of mixtures of precursors is possible generating solid solutions. Detailed analysis of both crystallographic (from XRD analyzed by Rietveld refinement) and local structure (from EXAFS analyzed by Reverse Monte Carlo simulations) provides evidence that it is possible to prepare nanocrystalline ZnO particles by chemical vapor synthesis where Co is substituting Zn in the wurtzite lattice which is the key requirement for the development of dilute magnetic semiconductors based on Co-doped ZnO. Sample preparation procedures and conditions play a very important role in obtaining Co-doped ZnO samples of high homogeneity and chemical vapor synthesis, as a nonequilibrium process where precursors are mixed on the molecular level in the gas phase, provides the possibility to prepare such samples.

Acknowledgments The authors gratefully acknowledge the generous support by the Collaborative Research Center SFB 445 ‘Nanoparticles from the Gas Phase’ funded by the German Research Foundation. We are also very thankful to Dr. Marina Spasova (team of Prof. Farle) and Dr. Ralf Theissmann (team of Prof. Schmechel) for providing the TEM imaging, Kerstin Brauner (team of Prof. Epple) for the determination of the chemical composition by atomic adsorption spectroscopy, Andreas Gondorf (team of Prof. Lorke) for the FTIR spectroscopy measurements and Dr. Adam Webb at HASYLAB/DESY for supporting us at beamline X1.

References

1. J.A. Rodriguez, M. Fernandez-Garcia, *Synthesis, Properties and Applications of Oxide Nanomaterials* (Wiley-Interscience, New York, 2007)
2. G.W. Kriechbaum, P. Kleinschmidt, *Adv. Mater.* **1**, 330 (1989)
3. A. Gutsch, H. Mühlenweg, M. Krämer, *Small* **1**, 31 (2005)
4. M. Winterer, *Nanocrystalline Ceramics—Synthesis and Structure* (Springer, Heidelberg, 2002)
5. I. Matsui, *J. Nanopart. Res.* **8**, 429 (2006)
6. M. Leskelä, M. Ritala, *Angew. Chem. Int. Ed.* **42**, 5548 (2003)
7. T. Masuda, S.R. Mukai, H. Fujikawa, Y. Fujikata, K. Hashimoto, *Mat. Manufact. Proc.* **9**, 237 (1994)
8. N.E. Pereira, X.W. Ni, *Chem. Eng. Sci.* **56**, 735 (2001)
9. N. Jongen, M. Donnet, P. Bowen, J. Lemaitre, H. Hofmann, R. Schenk, C. Hofmann, M. Aoun-Habbache, S. Guillemet-Fritsch, J. Sarrias, A. Rousset, M. Viviani, M.T. Buscaglia, V. Buscaglia, P. Nanni, A. Testino, J.R. Herguijuela, *Chem. Eng. Technol.* **26**, 303 (2003)
10. B.K.H. Yen, A. Günther, M.A. Schmidt, K.F. Jensen, M.G. Bawendi, *Angew. Chem. Int. Ed.* **44**, 5447 (2005)
11. M. Winterer, V.V. Srdic, R. Djenadic, A. Kompch, T.E. Weirich, *Rev. Sci. Instrum.* **78**, 123903 (2007)
12. O. Levenspiel, *Chemical Reaction Engineering* 3rd edn. (Wiley, New York, 1999)
13. M. Jakubith, *Chemische Verfahrenstechnik—Einführung in Reaktionstechnik und Grundoperationen* (VCH, New York, 1991)
14. L. Lutterotti, P. Scardi, *J. Appl. Cryst.* **23**, 246 (1990)

15. S.K. Friedlander, *Smoke, Dust, and Haze—Fundamentals of Aerosol Dynamics*, 2nd edn. (Oxford University Press, Oxford, 2000)
16. T.T. Kodas, S.K. Friedlander, *AIChE J.* **34**, 551 (1998)
17. G.-M. Chow, K.E. Gonsalves, *Nanotechnology—Molecular Designed Materials*, ACS Symposium Series, vol. 662 (American Ceramic Society, Washington, DC, 1996)
18. R.C. Flagan, M.M. Lunden, *Mat. Sci. Eng. A* **204**, 113 (1995)
19. X. Chen, S.S. Mao, *J. Nanosci. Nanotechnol.* **6**, 906 (2006)
20. G. Li, L. Li, J. Boerio-Goates, B. Woodfield, *J. Am. Chem. Soc.* **127**, 8659 (2005)
21. R. Djenadic, S.R. Chowdhury, M. Spasova, M. Gondorf, E. Akyildiz, M. Winterer, *Mater. Res. Soc. Symp. Proc.* **1056**, 1056-HH08-07 (2008)
22. K. Nakaso, K. Okuyama, M. Shimada, S.E. Pratsinis, *Chem. Eng. Sci.* **58**, 3327 (2003)
23. R.N. Grass, S. Tsantilis, S.E. Pratsinis, *AIChE J.* **52**, 1318 (2006)
24. T. Dietl, H. Ohno, F. Matsukura, J. Cibert, D. Ferrand, *Science* **287**, 1019 (2000)
25. K. Sato, H. Katayama-Yoshida, *Phys. E* **10**, 251 (2001)
26. M.J. Winterer, *Phys. IV* **7**, C2–243 (1997)
27. M. Winterer, *J. Appl. Phys.* **88**, 5635 (1988)
28. A.L. Ankudinov, B. Ravel, J.J. Rehr, R.C. Albers, S.D. Conradson, *Phys. Rev. B* **58**, 7565 (1998)
29. R. Djenadic, G. Akgül, K. Attenkofer, M. Winterer, *J. Phys. Chem. C* **114**, 9207 (2010)
30. S. Kolesnik, B. Dabrowski, J. Mais, *J. Appl. Phys.* **95**, 2582 (2004)
31. A.S. Risbud, N.A. Spaldin, Z.Q. Chen, S. Stemmer, R. Seshadri, *Phys. Rev. B* **68**, 205202 (2003)
32. L.B. Duan, W.G. Chu, J. Yu, Y.C. Wang, L.N. Zhang, G.Y. Liu, J.K. Liang, G.H. Rao, *J. Magn. Magn. Mater.* **320**, 1573 (2008)
33. V. Jayaram, J. Rajkumar, B.S. Rani, *J. Am. Ceram. Soc.* **82**, 473 (1999)
34. T.A. Schaedler, A.S. Gandhi, M. Saito, M. Rühle, R. Gambino, C.G. Levi, *J. Mater. Res.* **12**, 791 (2006)
35. B.B. Straumal, A.A. Mazilkin, S.G. Protasova, A.A. Myatev, P.B. Straumal, B. Baretzky, *Acta Mater.* **56**, 6246 (2008)
36. B. Straumal, B. Baretzky, A. Mazilkin, S. Protasova, A. Myatev, P. Straumal, *J. Eur. Ceram. Soc.* **29**, 1963 (2009)
37. Z. Sun, W. Yan, G. Zhang, H. Oyanagi, Z. Wu, Q. Li, W. Wu, T. Shi, Z. Pan, P. Xu, S. Wei, *Phys. Rev. B* **77**, 245208 (2008)

Nanoparticles from the Gasphase

Formation, Structure, Properties

Lorke, A.; Winterer, M.; Schmechel, R.; Schulz, C. (Eds.)

2012, XVIII, 418 p., Hardcover

ISBN: 978-3-642-28545-5